IOP Publishing Journal of Physics G: Nuclear and Particle Physics
J. Phys. G: Nucl. Part. Phys. **42** (2015) 034027 (13pp) doi:10.1088/0954-3899/42/3/034027

The impact of uncertain nuclear masses near closed shells on the *r*-process abundance pattern

M Mumpower[1], R Surman[1], D L Fang[2], M Beard[1] and A Aprahamian[1]

[1] Department of Physics, University of Notre Dame, Notre Dame, IN 46556 USA
[2] National Superconducting Cyclotron Laboratory, Michigan State University, East Lansing, MI 48824 USA

E-mail: rsurman@nd.edu

Received 17 August 2014, revised 26 September 2014
Accepted for publication 9 October 2014
Published 5 February 2015

Abstract

Calculations of rapid neutron capture nucleosynthesis involve thousands of pieces of nuclear data for which no experimental information is available. Of the nuclear data sets needed for *r*-process simulations—masses, β-decay rates, β-delayed neutron emission probabilities, neutron capture rates, fission probabilities and daughter product distributions, neutrino interaction rates—masses are arguably the most important, because they are a key ingredient in the calculations of all other theoretical quantities. Here, we investigate how uncertainties in nuclear masses translate into uncertainties in the final abundance pattern produced in *r*-process simulations. We examine the influence of individual mass variations on three types of *r*-process simulations—a hot wind, cold wind, and neutron star merger *r* process—with markedly different *r*-process paths and resulting final abundance patterns. We find the uncertainties in the abundance patterns due to the mass variations exceed the differences due to the astrophysics. This situation can be improved, however, by even modest reductions in mass uncertainties.

Keywords: *r*-process, nuclear masses, stellar elemental abundances

(Some figures may appear in colour only in the online journal)

1. Introduction

One of the major open questions in nuclear astrophysics is the origin of the heaviest element in rapid neutron capture, or *r*-process, nucleosynthesis. The solar system abundances of *r*-

process nuclei show three main peaks associated with the closed neutron shells at $N = 50$, 82, and 126. The locations of the peaks in A, $A \sim 80$, 130, and 195, indicate that they formed well away from stability, in conditions of high temperature and neutron density [1, 2]. Where these conditions are met astrophysically has still not been conclusively determined [3].

Many astrophysical sites have been proposed for the *r* process; see [4] and references therein. The two that have been most extensively investigated are the neutrino-driven wind of core collapse supernovae and the cold or mildly heated neutron-rich ejecta of neutron star mergers. A potential neutrino-driven wind *r* process depends on the still uncertain neutrino physics of the core collapse event; recent simulations suggest the outflows will not be driven sufficiently neutron rich for an *r* process to occur [5, 6]. Neutron merger outflows are predicted to be so neutron rich as to lead to fission recycling. However, galactic chemical evolution studies seem to show mergers cannot account for observations of *r*-process elements in very old stars [7, 8], unless early-onset mergers and instantaneous chemical mixing are assumed [9].

The suitability of a given astrophysical site is typically judged on its ability to produce *r*-process nuclei up to the third abundance peak at $A \sim 195$ [10]. However, potential *r*-process sites vary much more widely than just in the initial neutron-to-seed ratio. The location of the *r*-process path and the conditions during the decay of the neutron-rich products back to stability will be very different between, for example, a high-entropy, barely neutron-rich neutrino-driven wind and a low-entropy, low-electron fraction merger outflow. These differences are expected to leave imprints on the final abundance pattern produced [11].

In principle, we could use the details in the final abundance pattern to tell us about the location of the *r*-process path and the conditions in freezeout, which could then lead us to the appropriate *r*-process site. However, all *r*-process simulations use nuclear data for thousands of nuclei far from stability, only a small fraction of which is known experimentally. The details of the final abundance pattern have been shown to be sensitive to these individual pieces of nuclear data [12–18]. Thus, we expect our ability to tease out details of the astrophysical conditions from the abundance pattern is currently limited by uncertainties in nuclear physics.

Required pieces of nuclear data for the *r* process include masses, β-decay rates, β-delayed neutron emission probabilities, and neutron capture rates, with fission probabilities and daughter product distributions and neutrino interaction rates also potentially important depending on the astrophysical site. Of these, masses are arguably the most important, because the theoretical calculations of all other quantities depend on the masses. Theoretical mass models that extend from stability to the drip line, e.g., finite range droplet model (FRDM) [19], Duflo–Zuker (DZ) [20], Hartree–Fock–Bogoliubov (HFB) model—version 17 (HFB-17)—[21], and version 3 of the Woods–Saxon model (WS3) [22], all seem to do reasonably well predicting measured masses, with rms errors of 300–600 keV. However, away from measured values, the models diverge. Figure 1 shows an example of this, where the three mass models are compared to FRDM for the Erbium isotopic chain. Similar behavior is found for the mass models of every heavy element isotopic chain (see also figure 1 in [14, 15]), with large disagreements in excess of 1 MeV away from known values. The maximum difference between theoretical mass model predictions is shown for the entire nuclear chart in figure 2.

Here we examine the question: how do the uncertain masses of nuclei near closed shells impact the prediction of *r*-process abundances? To approach this question, we will use a self-consistent mass sensitivity study as in [24] to determine the changes in the *r*-process abundance pattern that result from each individual mass uncertainty. The sensitivity studies are described in section 2, with results presented in section 3 for separate studies of masses in the

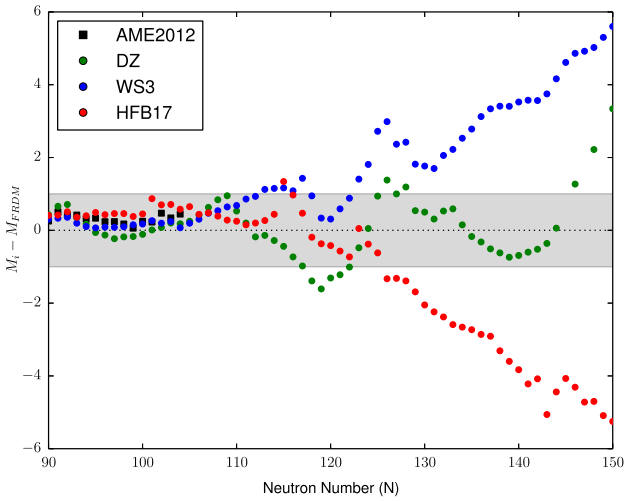

Figure 1. Difference between theoretical mass predictions from the FRDM [19] and the DZ [20] (green), HFB17 [21] (red), or WS3 [22] (blue) values for the Erbium ($Z = 68$) isotopes. Black squares shows the comparison with experiment, as evaluated in the AME2012 [23]. The gray band at ± 1 MeV shows the mass variation size for our sensitivity studies.

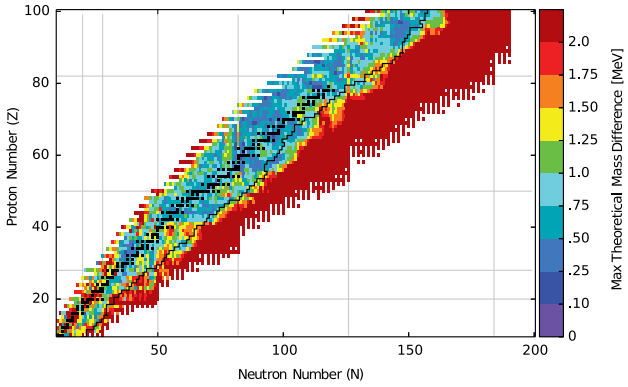

Figure 2. Maximum difference between theoretical nuclear mass model predictions (FRDM [19], DZ [20], HFB17 [21], and WS3 [22]) over the chart of nuclides. The black line shows the last neutron-rich mass to be measured and reported in the AME2012 [23].

$N = 82$ and $N = 126$ regions. In section 4, we show how we can use the results of the sensitivity studies to generate estimates of the resulting uncertainties in the final abundance patterns.

2. Mass sensitivity studies

One way to gauge the impact of an individual nuclear mass on the *r* process is to vary its value and look for resulting changes to the final abundance pattern produced in an *r*-process simulation. In an *r*-process sensitivity study, this is done systematically for every mass in a region of the nuclear chart.

A sensitivity study starts with a baseline *r*-process simulation that sets the choice of an astrophysical trajectory and nuclear physics inputs. Then, an individual piece of nuclear data —for example, a mass, β-decay rate, or neutron capture rate—is modified by a fixed amount, the simulation repeated, and the resulting abundance patterns compared. This step is repeated for each mass or reaction rate in a subset of the *r*-process network [12–18].

The mass sensitivity study of this work is similar to that described in [24]. We use a dedicated *r*-process network code from [13] that includes neutron capture, photodissociation, β decay, β-delayed neutron emission, and a schematic treatment of fission [25] for a nuclear network extending from stability to the neutron drip line for $A < 338$. Only a handful of the thousands of required pieces of nuclear data have been determined experimentally, thus we rely exclusively on theoretical tabulations for these quantities.

The nuclear mass models used most widely in calculations of Q values and reaction rates for the *r* process include FRDM [19], DZ model [20], and HFB models, e.g., [21]. The FRDM is a macroscopic–microscopic model employing a finite-range liquid-drop model for the macroscopic energy and a folded-Yukawa single-particle potential for the microscopic corrections. The latest version publically available [19] reports an rms error of 0.669 MeV compared to the masses known at the time (0.448 MeV for nuclei with $N \geqslant 65$). The DZ model is an alternate macroscopic–microscopic approach, with smaller rms errors (0.345 MeV) than the FRDM, but at the expense of a larger number of parameters fit to experimental masses. The HFB models, on the other hand, are fully microscopic, using Skyrme and realistic contact-pairing forces. The latest of these [26] fits the available mass data with rms deviations around 0.5 MeV. Still, the FRDM is arguably the most widely used, given the public availability of corresponding sets of neutron capture rates [27] and β-decay rates [28] calculated consistently with these masses.

For each of the mass models described previously, we recalculate neutron capture rates, β-decay rates, and β-delayed neutron emission probabilities to be consistent with the chosen mass model. For neutron capture, we use the freely available statistical model code TALYS [29] to recalculate the capture rates for the entire nuclear chart. We are careful to change the input parameters of TALYS that control the optical potential, gamma strength function, and level density model to ensure the rates are as fully consistent with each mass model as possible. For β decay, we use the spherical quasiparticle random phase approximation (QRPA) calculations of [30] for the β-decay rates and β-delayed neutron emission probabilities of nuclei around the $N = 82$ and $N = 126$ closed shells. The β-decay rates $\lambda_\beta = (2\pi/\hbar)\,|M_{if}|^2 \rho_f$ contain matrix element M_{if} and phase space ρ_f pieces, where the matrix element is the most computationally demanding portion to calculate and the phase space factor contains the dependence on the Q value. Thus, we start with two sets of matrix elements, calculated with the FRDM and HFB-17 masses, respectively, and recalculate the phase space factors consistently with the chosen mass model. The spherical QRPA calculations used here include first-forbidden transitions, which are important around closed shells; elsewhere we adopt the rates and probabilities of [28]. Our sensitivity studies start with baseline *r*-process simulations run with these sets of nuclear inputs.

The ability to generate nuclear inputs consistently with the masses is key to running the mass sensitivity studies. For each variation in an individual nuclear mass by a fixed ΔM, we

recalculate each piece of nuclear data that depends on this nuclear mass. For nucleus (Z, A), we recalculate the neutron separation energies of nuclei (Z, A) and $(Z, A + 1)$ using the definition $S_n = BE(Z, A) - BE(Z, A - 1)$ and the neutron capture rates of nuclei (Z, A) and $(Z, A - 1)$ using TALYS. Photodissociation rates are calculated via detailed balance with the modified capture rates and separation energies. To capture the largest part of the influence of the mass modification on the β-decay rates, we recalculate only the phase space factors ρ_f for nuclei (Z, A) and $(Z - 1, A)$ and adjust the appropriate β-decay lifetimes accordingly. Because the mass variation of nucleus (Z, A) alters the neutron separation energies of nuclei (Z, A) and $(Z, A + 1)$, we also recalculate the β-delayed neutron emission probabilities of nuclei $(Z - 1, A + j)$ where $j = 1 \ldots 4$. To keep our new QRPA calculations around the closed shells consistent with the rates and probabilities from [28], we limit to $j = 4$.

For each study, we choose an astrophysical trajectory, a nuclear mass model, and a region of the nuclear chart ($N \sim 82$ or $N \sim 126$) and run a baseline r-process simulation. We then vary a single nuclear mass, modify the nuclear inputs as described previously, and rerun the simulation. The resulting pattern of final isobaric mass fractions $X(A)$ is compared to the baseline abundance pattern for the same astrophysical trajectory $X_{\text{baseline}}(A)$ by computing the sensitivity measure F:

$$F = 100 \sum_A \left| X(A) - X_{\text{baseline}}(A) \right| . \tag{1}$$

These steps are repeated for each nuclear mass in the closed shell region, resulting in a set of sensitivity measures F that aim to capture the full impact of each mass on the final r-process abundances.

3. Sensitivity study results for the $N \sim 82$ and $N \sim 126$ regions

Figure 3 shows the results of three mass sensitivity studies run with the same baseline astrophysical trajectory and nuclear inputs from three different mass models for nuclei around the $N = 82$ shell closure. The baseline trajectory is a hot wind r process parameterized as in [31] with entropy $s/k = 200$, electron fraction $Y_e = 0.3$, and dynamical timescale $\tau = 80$ ms. This is a 'classic' hot (n, γ)–(γ, n) equilibrium r process without fission cycling. Thus, the location of the path during the equilibrium phase is set by the nuclear masses and so is expected to vary with the chosen mass model. Despite this, the pattern of sensitivity measures is similar in each case, with isotopes of cadmium, indium, tin, and antimony exhibiting the highest F values in all three studies. This conclusion is consistent with earlier work [14, 15], though these first studies considered only the impact of nuclear masses on setting the photodissociation rates and so underestimated the resulting sensitivity measures.

Although the exact location of the r-process path depends on the nuclear masses, the behavior of the r process will vary much more widely as a function of the astrophysical conditions. In figure 4, we compare the $N \sim 82$ mass sensitivity results from the hot wind case with FRDM inputs (top panel of figure 3) to studies run with three other astrophysical scenarios: a second hot wind r process with lower entropy of $s/k = 100$, a cold wind r process, and a neutron star merger simulation. The lower entropy of the second hot wind scenario does alter the r-process path, but only slightly in the $N = 82$ region. The resulting sensitivities are therefore quite similar for the two hot wind examples. In a cold r process, the temperature and density drop very quickly, such that photodissociation reactions rapidly fall out of equilibrium with captures. The r-process path is therefore pushed far from stability, where a new equilibrium between captures and β decays may be established. The cold r

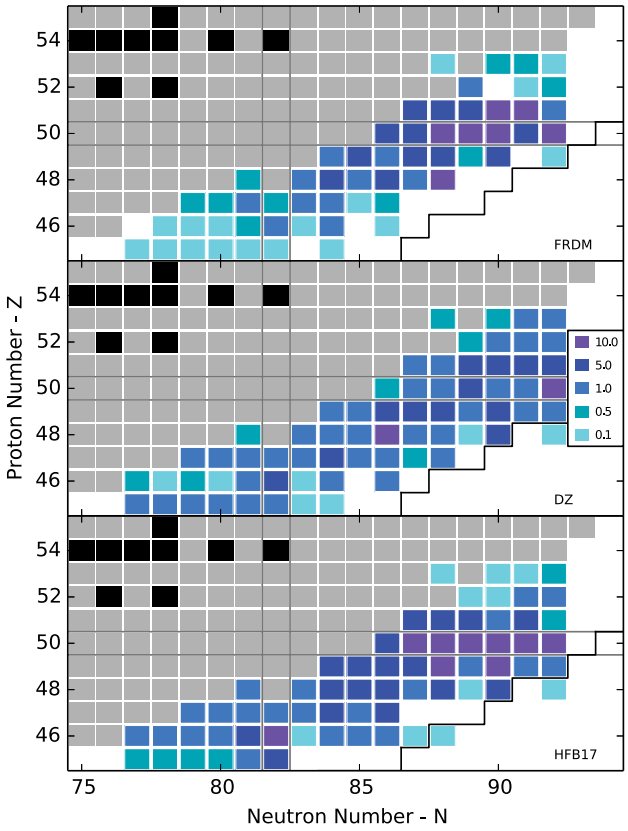

Figure 3. Maximum sensitivity measures $F_{\max}(Z, A)$ between ± 1.0 MeV mass variations near the $N = 82$ closed shell obtained in three sensitivity studies using hot wind r-process conditions ($s/k = 200$, $Y_e = 0.3$, $\tau = 80$ ms) and nuclear inputs based on the FRDM (top), DZ (middle), and HFB-17 (bottom) mass models. Overlaid in gray is the region of measured nuclear masses from AME2012 and black squares are stable isotopes. The solid black line represents the predicted 10^{-3} accessibility limit from the Facility for Rare Isotope Beams (FRIB).

process case here is a parameterized wind as in [32] with entropy $s/k = 150$, timescale $\tau = 20$ ms, and electron fraction $Y_e = 0.3$. The merger r-process simulation is from Bauswain and Janka as in [33]. The low Y_e, mildly heated ejecta produces a very neutron-rich (n, γ)–(γ, n) equilibrium r process with fission cycling. Thus, the latter two alternate scenarios result in r-process paths significantly farther from stability, which is reflected in the sensitivity study results. The tin and antimony isotopes show somewhat lower sensitivities in these trajectories, with higher sensitivities shifting to lower Z, silver and paladium. Still, in all cases, nuclear masses continue to shape how the r-process abundance pattern is finalized as material moves toward stability after equilibrium fails, so many of the same nuclei show sensitivities in all cases considered.

We extended our sensitivity calculations to nuclei around the $N = 126$ shell closure and find similar features in the pattern of sensitivity measures F for mass variations in this region. Figure 5 shows the results of three such sensitivity studies using the same baseline r-process

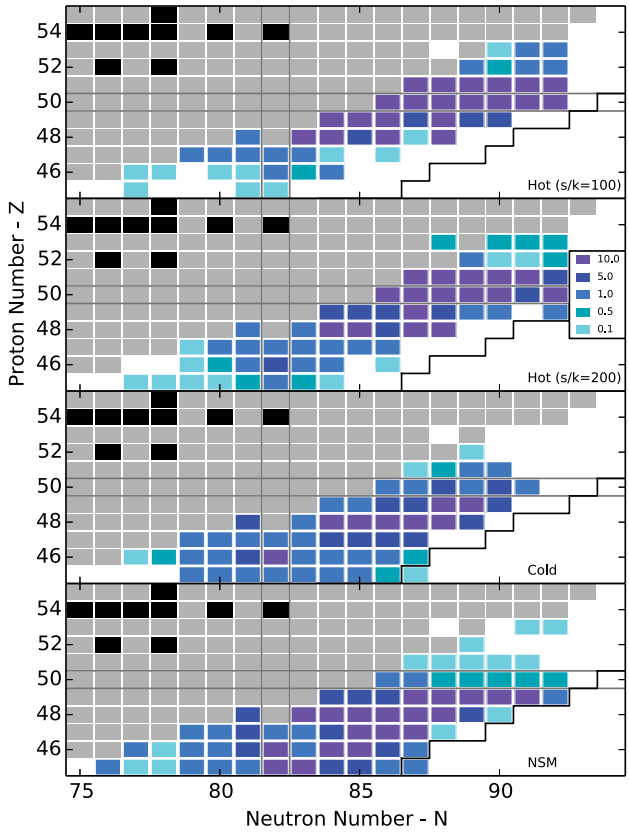

Figure 4. Maximum sensitivity measures $F_{\max}$ (Z, A) for nuclear masses near the $N = 82$ closed shell for four distinct *r*-process trajectories as described in the text. All four studies used mass variations of ± 1.0 MeV from FRDM. Overlaid in gray is the region of measured nuclear masses from AME2012 and black squares are stable isotopes. The solid black line represents the predicted 10^{-3} accessibility limit from FRIB.

simulations as in figure 4. Again, the highest sensitivity measures are obtained for nuclei at the closed shell, along the equilibrium *r*-process path, and along the decay pathways of the most populated equilibrium path nuclei.

4. Impact of individual mass variations on the abundance pattern

In the sensitivity studies described previously, individual nuclear mass variations can potentially alter the final abundance pattern through any one of the ingredients that depend on that nuclear mass. A change to a neutron separation energy can adjust the location of the equilibrium *r*-process path [14, 15]. A change to a β-decay Q value will modify the β-decay rate, which can in turn modify the nuclear flow between isotopic chains [16]. During the freezeout phase of the *r* process, when neutron capture, β decay, and possibly photodissociation all compete to set the final abundance pattern, a change to a mass can alter any of these quantities and thus the decay path to stability [12, 13, 17].

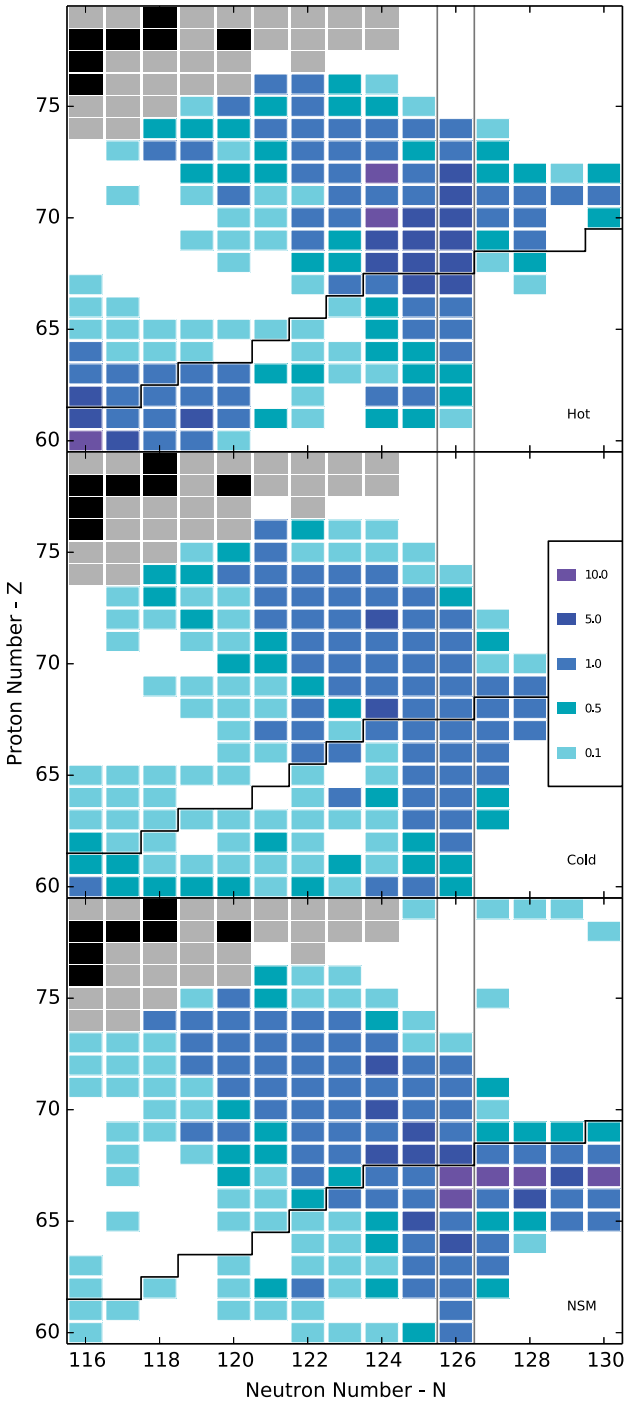

Figure 5. Maximum sensitivity measures $F_{\max}$ (Z, A) for nuclear masses near the $N = 126$ closed shell under various r-process trajectories. Details same as panels 2–4 from figure 4.

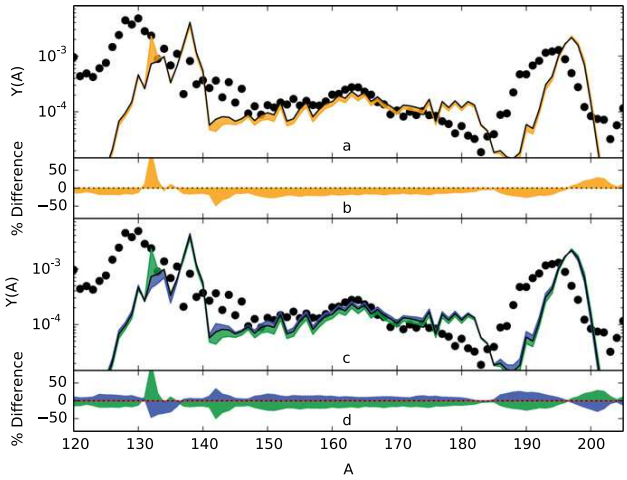

Figure 6. (a) The final abundance pattern $Y(A)$ vs A for the hot wind simulation in which the mass of ^{136}Cd is increased by 1 MeV and the mass variation is propagated to all affected nuclear physics quantities (yellow) compared to the baseline (black) and scaled solar data (black circles) from [34]. (c) Final abundance patterns from the separate simulations in which the mass change of ^{136}Cd is propagated through only the neutron capture rates (red), β-decay rates and β-delayed neutron emission probabilities (blue), or separation energies (green), compared to the baseline pattern (black). Panels (b) and (d) show the percent difference of the abundance patterns in (a) and (c), respectively.

An example of neutron separation energies impacting final abundances is shown in figure 6, for a mass variation of ^{136}Cd by 1 MeV in the hot wind sensitivity study with FRDM nuclear input. Figures 6(a) and (b) compare the baseline final abundance pattern to the abundance pattern produced with the ^{136}Cd mass variation propagated consistently through all pieces of nuclear data that depend on that mass. To determine which nuclear physics ingredient is primarily responsible for the change to the final abundance pattern, we repeat the simulation three times: once where the mass variation is propagated only to the neutron capture rates, once where the mass variation is propagated only to the weak decay properties, and once where only the appropriate neutron separation energies are adjusted. We note that in all cases where changes are propagated to neutron capture rates or separation energies, detailed balance is always preserved. The results shown in figures 6(c) and (d) indicate the change in the final abundance pattern seen in figures 6(a) and (b) is almost entirely due to the change to the neutron separation energies. This is because ^{136}Cd is on the equilibrium r-process path in the baseline simulation, and a mass variation shifts the location of the path away from this nucleus to ^{134}Cd.

The largest effect of a mass variation is not always its impact on the r-process path. Figure 7 shows an example where the abundance pattern changes are driven by the influence of the mass on the decay properties of a neighboring nucleus. Figure 7 is identical to figure 6, except the mass variation is a decrease to the mass of ^{140}Sb by 1 MeV. The mass modification of ^{140}Sb increases the β-decay rate of ^{140}Sn by a factor of 2. This produces an increase in the reaction flow from ^{140}Sn to ^{140}Sb, resulting in a shift in the path back to stability over a half second sooner than in the baseline simulation. This single change in reaction flow dramatically reduces the peak height found in the baseline, spreading this material to the rest of the pattern.

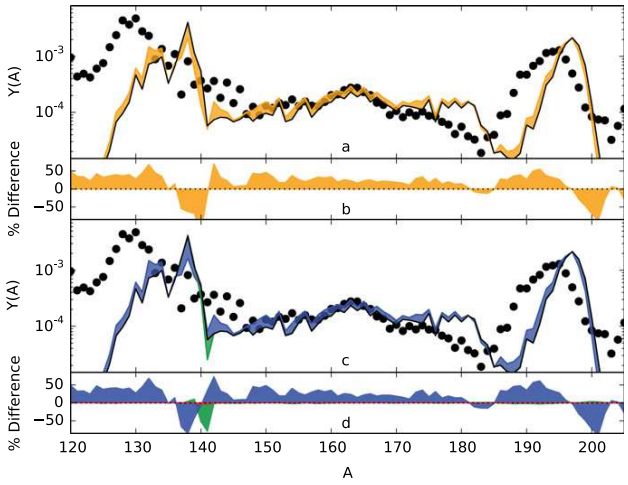

Figure 7. A different mechanism, in contrast to figure 6, showing the dominance of a β -decay effect that occurs when the mass of ^{140}Sb is decreased by 1 MeV.

5. Impact of all mass variations on the abundance pattern

We have discussed the impact of *individual* mass variations on final abundances on the order of $\Delta M = \pm 1$ MeV. Here, we address the larger question: how uncertain is the final abundance pattern produced by an *r*-process simulation due to the uncertainties in nuclear masses in the closed shell regions? If we accept that the closed shell masses are uncertain by at least an MeV, we can use our sensitivity study results to estimate the resulting error bars on the abundance pattern.

First, we combine the datasets of the $N = 82$ and $N = 126$ studies for the case of the FRDM mass model by selecting results for which $F > 1$. We next compute the average and variance of the abundances of this reduced set for each value of A, as shown in the blue curves of figure 8. To display outliers with this method, we also extract the maximum and minimum abundance for each value of A, indicated by the yellow lines in figure 8.

The final abundance patterns with variances thus calculated are shown in figure 8 for the example neutron star merger and hot wind scenarios. These two simulations have dramatically different *r*-process paths and freezeout dynamics, which influence the positioning, sizes, and widths of the abundance peaks. These abundance pattern features could in principle be used to constrain the *r*-process site, e.g., [11]. However, figure 8 suggests that the promise of this approach is currently restricted by uncertainties in nuclear masses. We reiterate that only uncertainties in nuclear masses near closed shells are considered when producing this figure. This means that the masses of nuclei around closed shells produce large uncertainties in *r*-process predictions throughout the final abundance pattern.

It is important to note that the ranges and variances shown in figure 8 are *underestimates* of the impact of nuclear data on the final *r*-process abundance pattern. The impact of masses between the closed shells is not shown, nor is the influence of other, larger uncertainties that plague calculations of reaction rates of nuclei far from stability. Neutron capture and photodissociation rates depend more sensitively on unknown level densities and the resulting gamma strength functions than nuclear masses, where different models result in rates that differ by up to many orders of magnitude [35]. Similar nuclear structure uncertainties affect

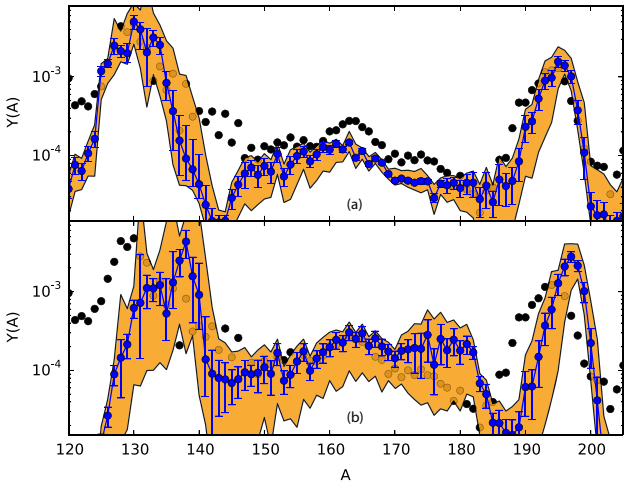

Figure 8. Uncertainty in final abundances for (a) the neutron star merger trajectory and (b) hot *r*-process trajectory based off the ±1 MeV variation of nuclear masses from FRDM. Masses were varied individually in both the $N = 82$ and $N = 126$ regions. The blue line and tick marks represent the average and standard deviation of all the mass variation simulations with $F > 1$. The yellow line represents the maximum and minimum abundance in these studies for each A.

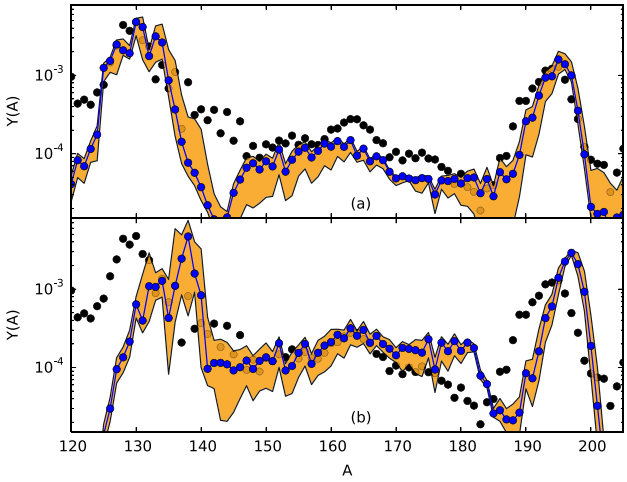

Figure 9. Uncertainty in final abundances for (a) the neutron star merger trajectory and (b) hot *r*-process trajectory based off a ±0.1 MeV variation of nuclear masses from FRDM. Details same as figure 8.

the β-decay matrix element calculations and resulting lifetime estimates [36]. The fission rates and daughter product distributions that shape the merger *r*-process pattern are possibly the most uncertain of all [33]. Coupling these observations with the abundance uncertainties

shown for ±1 MeV mass variation, we conclude that abundance uncertainties are currently too large to distinguish between the pattens produced by the two astrophysical environments.

This situation can be improved with reductions in nuclear mass uncertainties. To quantify this, we repeat the sensitivity studies used to create figure 8, using a mass variation of ±0.1 MeV instead of ±1 MeV. Figure 9 shows the final abundance patterns and variations that result. Here, the variations in the final abundance patterns are reduced sufficiently to see clear differences between the patterns produced by the two astrophysical scenarios, especially in the placement and sizes of the second and rare earth peaks. Again, these variations do not include the impact of uncertainties in masses between the closed shell regions, or nuclear structure effects on the reaction and decay rates. We plan to investigate these effects in future studies.

6. Conclusion

We have explored how individual variations as large as ±1 MeV and as low as ±0.1 MeV in nuclear masses near closed shells influence predictions of *r*-process abundances. Because masses are key inputs in all other relevant nuclear quantities, we propagate the mass variations to all nuclear properties that depend on that mass. Our results support the conventional picture that the most important nuclear masses lie along or near the *r*-process path. Additionally, we find individual pieces of nuclear data continue to shape the *r*-process pattern throughout the freezeout phase of the *r* process. Thus, the masses of nuclei between the *r*-process path and stability, particularly those along the decay pathways of the most populated equilibrium path nuclei, are also influential. Many of the same nuclei close to currently measured values show high sensitivity measures regardless of the nuclear mass model or astrophysical trajectory chosen for the sensitivity analysis.

Although we have not presented the equivalent to figures 3–5 for the ±0.1 MeV sensitivity studies, we note the pattern of F measures that results is the same as the ±1 MeV case. The principle difference between the two studies is simply the size of the abundance pattern variations produced.

From the sensitivity study results, we estimate the resulting uncertainties in the simulated *r*-process abundance pattern due to the mass variations. These uncertainties are considerable and dwarf differences in the final pattern predicted for different astrophysical sites. Thus, to develop the capacity to use details of the final abundance pattern to constrain the *r*-process astrophysical site, efforts to better pin down nuclear masses far from stability are required. Already reducing the mass variation by a factor of ten does reduce the abundance pattern variations to the point where some features of the hot wind and merger cases are distiguishable. However, this analysis does not include the impact of the much larger uncertainties in nuclear structure that enter the decay and reaction rates through the β and γ strength functions. These additional uncertainties will be the subject of future work.

Acknowledgments

This material is based upon work supported by the Joint Institute for Nuclear Astrophysics grant number PHY0822648 and the US Department of Energy Office of Science, Office of Nuclear Physics under Award Number DE-FG02-05ER41398.

References

[1] Burbidge E M, Burbidge G R, Fowler W A and Hoyle F 1957 *Rev. Mod. Phys.* **29** 547–650
[2] Cameron A G W 1957 *Publ. Astron. Soc. Pac.* **69** 201–22
[3] Arnould M, Goriely S and Takahashi K 2007 *Phys. Rep.* **450** 97–213
[4] Thielemann F K *et al* 2011 *Prog. Part. Nucl. Phys.* **66** 346–53
[5] Roberts L F, Reddy S and Shen G 2012 *Phys. Rev.* C **86** 065803
[6] Martínez-Pinedo G, Fischer T and Huther L 2014 *J. Phys. G: Nucl. Part. Phys.* **41** 044008
[7] Mathews G J and Cowan J J 1990 *Nature* **345** 491–4
[8] Argast D, Samland M, Thielemann F K and Qian Y Z 2004 *Astron. Astrophys.* **416** 997–1011
[9] Matteucci F, Romano D, Arcones A, Korobkin O and Rosswog S 2014 *Mon. Not. R. Astro. Soc.* **438** 2177–85
[10] Meyer B S and Brown J S 1997 *Astrophys. J. S.* **112** 199–220
[11] Mumpower M, McLaughlin G C and Surman R 2012 *Astrophys. J.* **752** 117
[12] Surman R, Beun J, McLaughlin G C and Hix W R 2009 *Phys. Rev.* C **79** 045809
[13] Mumpower M, McLaughlin G C and Surman R 2012 *Phys. Rev.* C **86** 035803
[14] Brett S, Bentley I, Paul N, Surman R and Aprahamian A 2012 *Euro. Phys. J.* A **48** 184
[15] Aprahamian A, Bentley I, Mumpower M and Surman R 2014 *AIP Advances* **4** 041101
[16] Mumpower M, Cass J, Passucci G, Surman R and Aprahamian A 2014 *AIP Advances* **4** 041009
[17] Surman R, Mumpower M, Sinclair R, Jones K L, Hix W R and McLaughlin G C 2014 *AIP Advances* **4** 041008
[18] Surman R, Mumpower M, Cass J, Bentley I, Aprahamian A and McLaughlin G C 2014 *EPJ Web Conf.* **66** 7024
[19] Möller P, Nix J R, Myers W D and Swiatecki W J 1995 *At. Data Nucl. Data Tables* **59** 185–381
[20] Duflo J and Zuker A P 1995 *Phys. Rev.* C **52** R23–7
[21] Goriely S, Chamel N and Pearson J M 2009 *Phys. Rev. Lett.* **102** 152503
[22] Wang N and Liu M 2013 *J. Phys.: Conf. Ser.* **420** 012057
[23] Wang M, Audi G, Wapstra A H, Kondev F G, MacCormick M, Xu X and Pfeiffer B 2012 *Chin. Phys.* C **36** 1603–2014
[24] Mumpower M, Fang D-L, Surman R, Beard M and Aprahamian A 2014 arXiv:1410.7275
[25] Beun J, McLaughlin G C, Surman R and Hix W R 2008 *Phys. Rev.* C **77** 035804
[26] Goriely S, Chamel N and Pearson J M 2013 *Phys. Rev.* C **88** 024308
[27] Rauscher T and Thielemann F K 2000 *At. Data Nucl. Data Tables* **75** 1–351
[28] Möller P, Pfeiffer B and Kratz K L 2003 *Phys. Rev.* C **67** 055802
[29] Goriely S, Hilaire S and Koning A J 2008 *Astron. Astrophys.* **487** 767–74
[30] Fang D L, Brown B A and Suzuki T 2013 *Phys. Rev.* C **88** 034304
[31] Meyer B S 2002 *Phys. Rev. Lett.* **89** 231101
[32] Panov I V and Janka H T 2009 *Astron. Astrophys.* **494** 829–44
[33] Goriely S, Sida J L, Lemaître J F, Panebianco S, Dubray N, Hilaire S, Bauswein A and Janka H T 2013 *Phys. Rev. Lett.* **111** 242502
[34] Arlandini C, Käppeler F, Wisshak K, Gallino R, Lugaro M, Busso M and Straniero O 1999 *Astrophys. J.* **525** 886–900
[35] Beard M, Uberseder E, Crowter R and Wiescher M 2014 *Phys. Rev.* C **90** 034619
[36] Sarriguren P and Pereira J 2010 *Phys. Rev.* C **81** 064314